NANO LETTERS

pubs.acs.org/NanoLett
Letter

Pressure-Tunable Phase Transitions in Atomically Thin Chern Insulator $MnBi_2Te_4$

Albin Márffy, Endre Tóvári,* Yu-Fei Liu, Anyuan Gao, Tianye Huang, László Oroszlány, Kenji Watanabe, Takashi Taniguchi, Su-Yang Xu, Péter Makk,* and Szabolcs Csonka

Cite This: *Nano Lett.* 2026, 26, 1782−1788
Read Online

ABSTRACT: Topological insulators lacking time-reversal symmetry can exhibit the quantum anomalous Hall effect. Odd-layer thick $MnBi_2Te_4$ is a promising platform due to its intrinsic magnetic nature; however, quantization is rarely observed in it. Our magnetoresistance measurements in the antiferromagnetic phase indicate, instead of a quantum anomalous Hall insulator, the presence of a trivial insulator state likely due to disorder, while in a high magnetic field, a Chern insulator state appears. From the magnetic field and temperature dependence, we estimate that the interlayer exchange coupling is enhanced by hydrostatic pressure while the intralayer coupling is weakened. The trivial band gap is also reduced, suggesting the role of disorder is weakened upon compression of the layers.

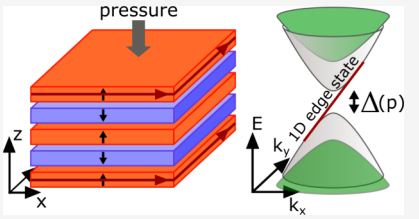

KEYWORDS: *topological magnets, pressure-induced phase transition, Chern insulator, topological phase transition*

INTRODUCTION

For the quantum anomalous Hall effect (QAHE), a material exhibits a quantized Hall resistance without an external magnetic field, which requires the presence of an intrinsic magnetization that breaks time-reversal symmetry.[1,2] This effect arises in topological insulators with ferromagnetic order, leading to dissipationless chiral edge states, while the bulk remains insulating. Spatially manipulating such spin-polarized modes is expected to be part of producing novel quantum bits.[3]

$MnBi_2Te_4$ (MBT) is a particularly promising material for the realization of the QAHE because it is an intrinsic magnetic topological insulator,[4−6] as it naturally combines both topological and magnetic properties without requiring external doping. It is an A-type antiferromagnet (AFM) wherein the magnetization alternates across and is perpendicular to the septuple atomic layers (SLs),[4,7] as shown in Figure 1a. As van der Waals materials, MBT and related compounds are predicted to be easier to fabricate and control than topological materials doped with magnetic impurities, and they host a wide variety of topological quantum states.[8,9] Due to the exchange interaction related to the magnetization of the surface layers, the two-dimensional (2D) topological surface states become gapped, as illustrated in Figure 1b. If the Fermi level is tuned into the gap, one-dimensional chiral modes may propagate along the edges of the flake.

The characteristics of thin MBT films depend on the number of SLs and the magnetic phase.[10] In the AFM phase, if the Fermi level is in the gap, odd (even)-SL MBT is expected to exhibit a quantum anomalous Hall (axion) insulator state with unity (zero) Chern number C, and the Hall resistance is quantized as $|R_{xy}| = h/e^2$[1,11−13] (zero[4,6,9,12,14]), where h is

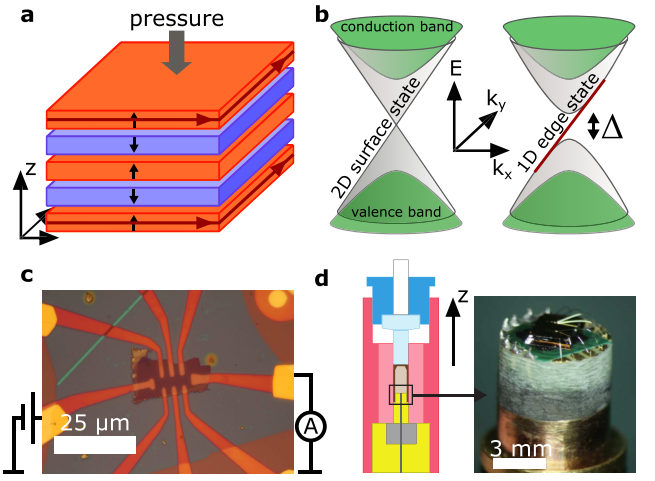

Figure 1. (a) A-Type AFM order for the five SLs. Black arrows represent the SL magnetizations, and dark red arrows the chiral edge states. (b) Illustration of the surface state Dirac cone without (left) and with (right) a topologically nontrivial exchange gap. (c) Optical image of the device. Source and drain contacts are indicated, while the electrical setup of side contacts varied based on the requirements. (d) Schematic of the pressure cell and photo of the PCB carrying the chip.

Received: November 7, 2025
Revised: December 30, 2025
Accepted: January 13, 2026
Published: January 29, 2026

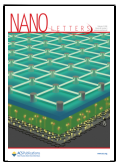

https://doi.org/10.1021/acs.nanolett.5c05229
Nano Lett. 2026, 26, 1782−1788

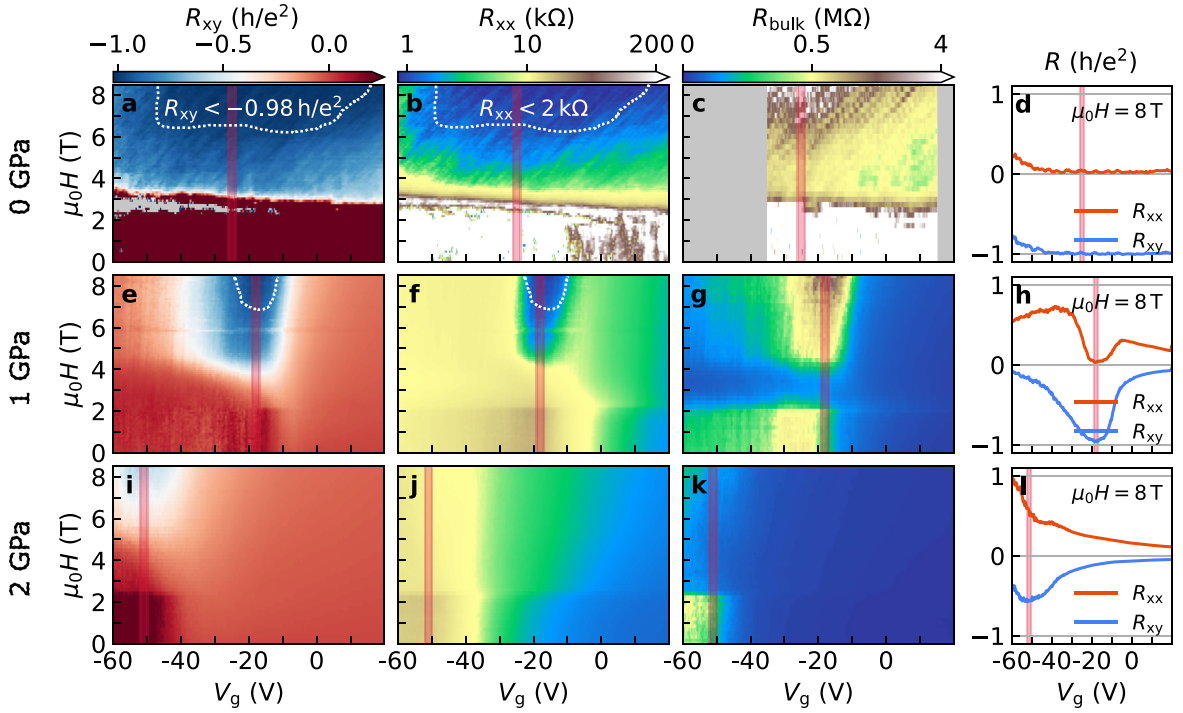

Figure 2. Magnetoresistance at a series of pressures. (a) Map of the Hall (R_{xy}), (b) longitudinal (R_{xx}), and (c) bulk (R_{bulk}) resistance as a function of gate voltage (V_g) and out-of-plane field $\mu_0 H$ at 1.5 K and 0 GPa. (d) Corresponding horizontal cuts at $\mu_0 H$ = 8 T of R_{xx} (red) and R_{xy} (blue). The same at (e−h) 1 and (i−l) 2 GPa. The CNP estimated at each pressure is marked by red vertical lines. Areas outlined by white dashed lines in panels a and e mark where $R_{xy} \leq -0.98\ h/e^2$ and in panels b and f where $R_{xx} \leq 2$ kΩ. For the sake of clarity, the color scale of R_{xx} and R_{bulk} has two linear slopes, with centers at 10 kΩ and 0.5 MΩ, respectively.

Planck's constant and e is the elementary charge. In a high out-of-plane magnetic field H, the layers are fully polarized in a ferromagnetic (FM) phase, and R_{xy} is similarly quantized in a Chern insulator (CI) state with |C| = 1, irrespective of the number of SLs.[9,11,15−21]

However, the QAHE in odd-SL samples is often absent, and quantization may occur only in the field-polarized FM phase. Instead, a wide range of electronic properties has been observed at low field, for example, a topologically trivial insulator state with near-zero R_{xy}.[17,19,20,22,23] This discrepancy may be related to variations in material quality due to defects or surface degradation,[13,24−28] potentially affecting the magnetic interactions.[29,30] Therefore, the goal of this study is to investigate the tunability of the magnetic interactions and the complex phase diagram by reducing the interlayer distance by applying pressure.[31] We performed magnetoresistance measurements on five-SL MBT samples that lack the QAHE plateau. We studied phase transitions as a function of the magnetic field and the band gaps through thermal activation measurements. We found that the system is highly tunable with pressure p. The trivial zero-field band gap is reduced by an increase in p, while the CI band gap is weakly affected; moreover, the onset field of the FM phase increases. These observations are consistent with an increase in the interlayer AFM coupling, while the role of disorder appears to be weakened upon compression of the layers.

EXPERIMENTAL RESULTS

The sample geometry is shown in Figure 1c. The device (detailed in Methods) was fabricated in a glovebox. All MBT samples were protected from air and solvents throughout the whole process. The chip was attached and wire-bonded to a PCB as described in ref 31 and then loaded into a hydrostatic pressure cell as demonstrated in Figure 1d. Measurements were carried out in a liquid helium cryostat equipped with a variable-temperature insert, using a low-frequency lock-in technique. The doped Si/SiO_2 substrate served as a gate electrode/dielectric. The pressure was applied at room temperature and set for each cool-down. In the test, we show results collected from sample B. Additional data collected on sample A, showing similar trends, can be found in the Supporting Information.

Electronic Phases

First, we discuss the gate voltage (V_g) and external magnetic field (H) dependence of the Hall, longitudinal, and bulk resistances at pressures of approximately 0, 1, and 2 GPa, as shown in Figure 2. R_{bulk} was measured by grounding the contacts on both sides of the Hall bar (the three top and three bottom leads in Figure 1c) between the source and drain, effectively eliminating potential edge state contributions to the current.

Panels b and c of Figure 2 plot R_{xx} and R_{bulk}, respectively, as a function of V_g and H at 0 GPa. Their values up to about $\mu_0 H$ = 3 T are in the range of hundreds of kiloohms and several megaohms, respectively. This demonstrates that the device is highly resistive in the studied gate range and that there are no edge states, as they would lead to an R_{xx} below a few kiloohms. Hall resistance R_{xy}, shown in Figure 2a, reaches several h/e^2 in the same region (dark red area), which is caused by mixing with the large R_{xx} due to the irregular shape of the sample. These observations indicate a topologically trivial insulator state at low fields, similar to the findings of refs 17 and 22. The insulating character is also supported by measurements of R_{xx} as a function of temperature T (see Figure S4).

https://doi.org/10.1021/acs.nanolett.5c05229
Nano Lett. 2026, 26, 1782−1788

In contrast, above around $\mu_0 H = 6$ T, the Hall signal becomes quantized, $R_{xy} \approx -h/e^2$, while R_{xx} decreases close to zero, consistent with a CI state. This region is marked by white dashed lines in panels a and b of Figure 2 and is also demonstrated in panel d as horizontal cuts at 8 T. We estimate the position of the charge neutrality point (CNP) as approximately −25 V and highlight it by vertical red lines in the figure. The presence of a CI state is supported by the increase in R_{bulk} at the CNP at high field (Figure 2c), as well as T dependence (Figure.S4). In the regime between the trivial and Chern insulator states (∼3−6 T), the reduced R_{bulk} suggests a closure or decrease in the bulk band gap, and further discussion of the origin of this phenomena can be found in the Discussion. The quantum Hall effect (QHE) can be ruled out as no fan-like features are visible on the color map, and the sign of R_{xy} does not change with V_g at high field.

When the pressure is increased to 1 GPa, features similar to those described above are observed, except in a narrower V_g range around a CNP of −18 V, as demonstrated in Figure 2e−h. At low field, R_{xx} and R_{bulk} are relatively large, though not as high as at 0 GPa, while R_{xy} is on the order of 0.1 h/e^2. Including the T dependence in Figure S5, these indicate that the system is still a trivial insulator. When the field is increased above ∼2 T, the bulk resistance decreases and then, after an intermediate regime, increases again. This is accompanied by a significant reduction in R_{xx}, while R_{xy} reaches $-h/e^2$, heralding the appearance of the nontrivial (CI) state. These areas are again highlighted by white dashed lines. On either side of this V_g range, the Fermi level is tuned into the valence or conduction bands and the CI quantization disappears (Figure 2h). Compared to the 0 GPa case, the smaller width of insulating or quantized regions along the V_g axis suggests a decrease in the band gaps or a reduced density of defects.

At 2 GPa (Figure 2i−l), the low-field trivial insulating state is still present with an even lower resistance (see also Figure S6), while the CNP is shifted to −51 V. A quantized R_{xy} and near-zero R_{xx} were not observed up to 8.5 T. Nevertheless, there is a peak in R_{bulk} in the CNP at high field, and the features in R_{xy} are similar to the maps at lower pressures. Their tendencies with V_g and H suggest that the FM phase and the corresponding CI state form at magnetic fields that are out of the range of the measurements.

Magnetic Phases

The longitudinal magnetoresistance and, especially, the anomalous Hall resistance make it possible to determine the magnetic phase transitions. We interpret them in the framework of a linear chain model[11,17,29,30,32] with the energy function

$$E \propto H_E \sum_{j=2}^{5} \mathbf{M}_j \mathbf{M}_{j-1} - \frac{H_a}{2} \sum_{j=1}^{5} {M_{j,z}}^2 - H \sum_{j=1}^{5} M_{j,z} \qquad (1)$$

detailed in the Supporting Information. Here, $H_E > 0$ is the interlayer AFM exchange in units of amperes per meter, $H_a > 0$ is the anisotropy that defines the easy (out of plane, z) axis, and $\mathbf{M}_j$ is dimensionless layer magnetizations of unit length.

We plot H sweeps of the symmetrized longitudinal resistance $R_{xx(S)}$ and antisymmetrized Hall resistance $R_{xy(AS)}$ close to the CNP in panels a and b of Figure 3. Near zero field, the system is in one of two mirror-symmetric AFM states, illustrated in the bottom of Figure 3d. As the field is increased (black curves in Figure 3), around $\mu_0 H = 1$ T a small decrease

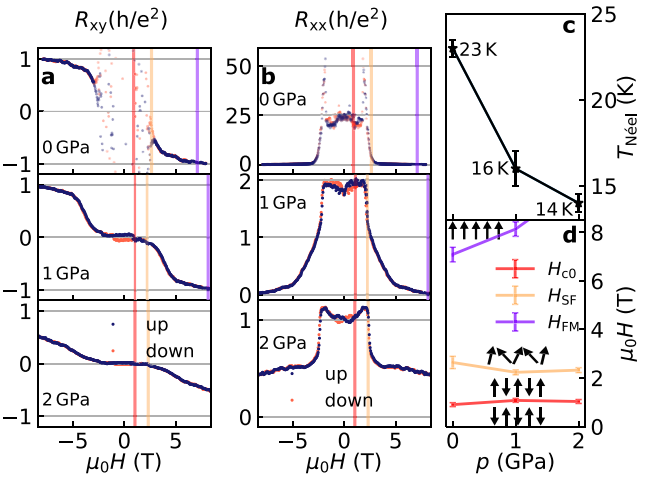

Figure 3. Magnetic transitions. (a) Up (black) and down (red) field sweeps of the antisymmetrized Hall resistance and (b) symmetrized longitudinal resistance (see eqs S1 and S2) close to the CNP for all pressures at 1.5 K. (c) Néel temperature vs pressure based on $R_{xx}(T)$ or its derivative (see Figure S2). (d) Estimated transition fields between the magnetic phases vs pressure, as highlighted by colored lines in panels a and b. The orientation of the SL magnetizations between them is illustrated by black arrows.

in R_{xy} can be observed at most pressures, highlighted by vertical red lines. This is part of a hysteresis loop between the up and down sweeps (black and red curves, respectively) and is most prominent at 1 GPa. The gate dependence of its magnitude is plotted in panels a and c of Figure 4 and will be

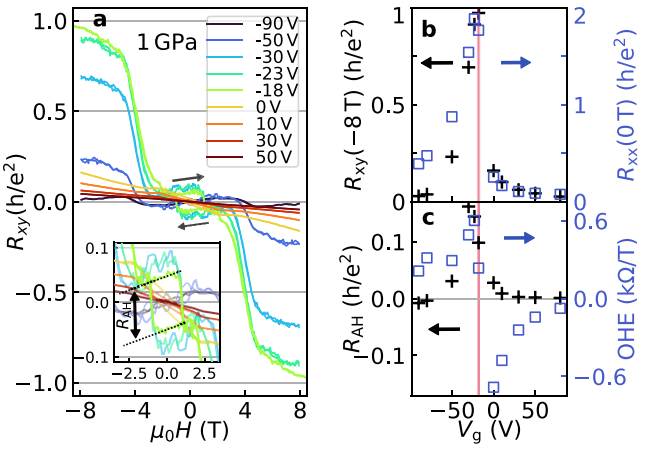

Figure 4. AHE at 1 GPa and 1.5 K. (a) Antisymmetrized R_{xy} as a function of H at a series of gate voltages. The inset shows a close-up of the data, where the dotted lines are linear fits to one of the loops. (b) R_{xy} at −8 T (black markers) and R_{xx} at 0 T (blue) as a function of V_g. The CNP is marked by a red line. (c) Size R_{AH} of the hysteresis loop (black symbols) and the ordinary Hall coefficient (OHE, in blue) at low field.

discussed further below. It is attributed to the first-order phase transition between the two AFM states and can be observed via the anomalous Hall effect (AHE). This complete flip of the magnetization of all SLs occurs at field H_{c0} when the Zeeman energy of the net magnetization becomes large enough compared to AFM exchange H_E and anisotropy H_a. At 2 GPa, a smaller hysteresis loop can be observed (see also Figure S1a,c), while for 0 GPa, its edge H_{c0} could only be determined

https://doi.org/10.1021/acs.nanolett.5c05229
Nano Lett. 2026, 26, 1782−1788

through conductivity σ_{xy} (displayed in Figure S3) due to the contribution of a divergent and noisy R_{xx} to R_{xy}.

Starting from the energetically favorable AFM state above H_{c0}, further increasing the field produces a suddenly sloping $R_{xy}(H)$ and a decrease in $R_{xx}(H)$ for all pressures as highlighted by vertical orange lines (H_{SF}) in panels a and b of Figure 3. The transition can also easily be identified in the non-symmetrized maps of R_{bulk} in Figure 2 near 2−3 T. It is attributed to the spin-flop transition to the canted antiferromagnetic (cAFM) state, which is illustrated by the tilted arrows in Figure 3d. Here all layer magnetizations are partially aligned with the magnetic field, as it dominates the anisotropy, but it still competes with the exchange H_E.

Above 7 T, R_{xy} and R_{xx} saturate around $-h/e^2$ and zero, respectively, as shown in panels a and b of Figure 3 for 0 and 1 GPa. We highlight these fields (H_{FM}) by vertical purple lines and attribute them to the onset of FM order and the CI state.[11,17] The transition fields between the phases are plotted in Figure 3d with colors corresponding to the vertical lines in panels a and b. The onset field of the FM phase (H_{FM}, purple symbols) is much larger than that of the cAFM phase (H_{SF}, orange) and moves out of range at 2 GPa.

We extracted Néel temperature T_N, which is revealed by a local maximum in $R_{xx}(T)$ or can be determined from its derivative (see the Supporting Information and Figure S2), and we show the results in Figure 3c. The estimated value of 0 GPa of 23 K closely matches the values in the literature.[5,17] T_N decreases with an increase in pressure, which is consistent with ref 33.

Next, we present the magnitudes of AHE at low and high fields. Figure 4 summarizes the magnetotransport data collected at 1.5 K and 1 GPa (the 2 GPa set is similar (see Figure S1)). In panel a, the antisymmetrized Hall resistance is shown for several gate voltages. As already mentioned in relation to Figure 3, a fully quantized R_{xy} can be observed at large $|H|$ at −18 V, the CNP. Away from the CNP, high-field Hall resistance R_{xy} (−8 T) decays toward zero as plotted in Figure 4b by black markers. The fact that its sign is independent of V_g confirms that the plateau is unrelated to the QHE. The position of the peak in R_{xx}(0 T) versus V_g, which is plotted in the same panel in blue symbols, is consistent with the CNP as expected of a low-field insulator state.

In the inset of Figure 4a, a magnified view of the data at low $|H|$ is plotted, showing the AHE hysteresis loops. The black dashed lines are linear fits of the −23 V Hall signal. Their vertical distance characterizes the size of the AHE loop, R_{AH}, as highlighted by the vertical arrow, while their slope gives the ordinary Hall coefficient (OHE). We have estimated these quantities at several gate voltages and plot them in Figure 4c. The low-field OHE (blue markers) crosses zero sharply at the CNP while its magnitude is largest near here. This is consistent with a continuous change from hole to electron transport, marking a difference between the trivial insulator state here and the axion insulator state in even-SL MBT, where it has been suggested that the OHE exhibits a plateau at zero as a function of V_g near the CNP.[9,27]

R_{AH} (black markers in Figure 4c) is largest close to the CNP and decays fast with V_g on both sides. It changes sign in the hole regime, which is most apparent in the curves at 2 GPa (see the inset of Figure S1a). In other words, at this doping, the low-field AHE signal depends on the net magnetization opposite the high-field case.

Temperature Dependence

In order to study the nature of the different insulating states as the system is tuned by hydrostatic pressure, we performed temperature-dependent measurements. In Figure 5a, R_{bulk} is

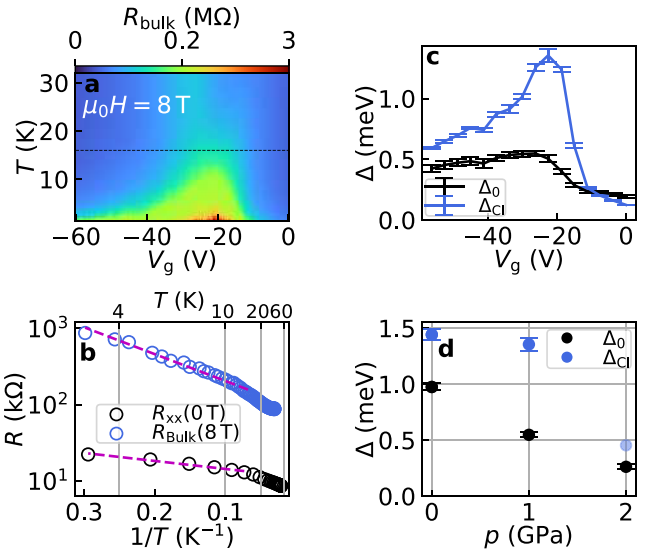

Figure 5. Thermal activation in the trivial and Chern insulator states. (a) Bulk resistance measured at 1 GPa and $\mu_0 H$ = 8 T as a function of gate voltage and temperature. For the sake of visibility, the color scale has two linear slopes, with the center at 0.2 MΩ. The black dashed line indicates a T_N of 16 K. (b) Arrhenius plot of the 0 T longitudinal (black) and 8 T bulk resistances (blue, from panel a) at the CNP. The dashed lines correspond to linear fits of the data below T_N. (c) Thermally activated gap sizes below T_N as a function of V_g at 1 GPa. Black and blue markers were obtained from $R_{xx}(T)$ and $R_{bulk}(T)$ at 0 and 8 T, respectively, and thus correspond to the trivial (Δ_0) and CI (Δ_{CI}) gap, respectively. (d) Maximal values of Δ_0 and Δ_{CI} at all pressures.

shown as a function of V_g and T in the FM phase at $\mu_0 H$ = 8 T and 1 GPa. It exhibits a maximum value centered near the CNP for all values of T. Moreover, it increases with a decrease in temperature, as illustrated by the vertical cut in the CNP in Figure 5b, confirming the presence of a gap in the CI state, Δ_{CI}. As for the trivial insulator state, we focus on longitudinal resistance R_{xx} at 0 T. Figure 5b shows its T dependence in the CNP, which enables estimation of trivial insulator band gap Δ_0. Other measurements for all pressures can be found in the Supporting Information.

The gaps were estimated through Arrhenius analysis at all gates, and the results at 1 GPa are plotted in Figure 5c. Both Δ_0 and Δ_{CI} are maximal close to the CNP. The pressure dependence of their peak values is plotted in Figure 5d. The CI gap is more robust than the trivial gap for all pressures. Δ_{CI} at 2 GPa is likely underestimated, since the FM phase has not yet formed at 8 T. Rather, we expect that it is comparable to the value at 1 GPa. The 0 and 1 GPa points for Δ_{CI} are in the FM phase, and their slowly decreasing trend likely reflects the behavior of the exchange interaction component of the CI gap. In contrast, trivial gap Δ_0 is significantly suppressed by the pressure.

DISCUSSION

Altogether, our experimental results show the Chern insulating state at a high field. This state appears in the ferromagnetic

https://doi.org/10.1021/acs.nanolett.5c05229
Nano Lett. 2026, 26, 1782−1788

phase and forms at larger magnetic fields as the pressure is increased. Our results also show the presence of a trivial insulator state in the AFM phase instead of the QAHE features expected in odd-SL MBT. Ideally, the parallel magnetization of the top and bottom surface layers opens a sizable gap in the topological surface states that, according to theoretical calculations, is on the order of 80 meV.[11,25] Hence, in simple terms, the characteristic energy scale of QAHE is the exchange energy. However, the gaps extracted are more than 1 order of magnitude smaller. We believe that the absence of the QAHE might be explained in terms of a reduced exchange energy, although the exact mechanism is up for debate.

One possibility that is in good agreement with our measurements is that nontrivial exchange gap Δ_A of the AFM state, already strongly weakened by Mn_{Bi} antisite defects as indicated in ref 25, is surpassed by a sufficiently strong disorder potential. This would ultimately lead to a trivial insulator phase,[34] which has an effective transport gap (Δ_0). Consequently, intrinsic anomalous Hall conductivity σ_{xy} is effectively reduced to near zero (see Figure S3) and strong localization occurs. With an increase in the magnetic field, transitions occur to the cAFM and then to the FM phase. FM exchange gap Δ_{CI} might be larger than Δ_A of the AFM phase, since the exchange field is larger if all layers are aligned (discussed further below)[11] or because an external magnetic field may polarize the Mn antisite defects, effectively increasing the magnetization of each layer.[25] Hence, Δ_{CI} could dominate the disorder (on the order of Δ_0), and thus, a magnetic field can induce a quantum phase transition and allow Hall quantization matching our observations. Accordingly, in panels a and b of Figure 3, the change in the slope of R_{xy} and the decrease in R_{xx} at the spin-flop (AFM to cAFM) transition at H_{SF} indicate the departure from the trivial insulator state and the reappearance of a large intrinsic σ_{xy}.

The anomalous Hall effect in the AFM state is indeed weak, and interestingly, its magnitude R_{AH} changes sign when V_g is tuned as shown in Figure 4c. This is even more pronounced at 2 GPa, as shown in panels b and c of Figure S1. The sign reversal of the AHE in Cr-doped $Bi_2(Se_xTe_{1-x})_3$ samples has been experimentally observed before and is explained in terms of intrinsic AHE in a disordered system.[35] Another explanation for the sign reversal is an extrinsic origin for AHE.[22] In any case, the presence of the gate-tunable sign reversal of the AHE supports the possibility of the important role of disorder.

We have analyzed the magnetic transition fields shown in Figure 3d based on the linear chain model (see the Supporting Information). The fact that the spin-flip (cAFM/FM) transition occurs at fields much higher than those of the AFM/AFM/cAFM transitions ($H_{FM} \gg H_{c0}$ and H_{SF}) suggests that easy axis anisotropy field H_a in eq 1 is significantly weaker than antiferromagnetic interlayer exchange H_E (see Figure S7b) at all pressures. Moreover, H_{FM} increases as a function of pressure while H_{c0} and H_{SF} remain approximately constant. Based on the model, this is only possible if H_E increases and H_a decreases with pressure (see the Supporting Information). This result is consistent with expectations;[23,33] the former can be attributed to the compression along the c axis, and the latter may be the result of the reduced distance of nearest-neighbor Mn atoms due to the compression in the $a-b$ plane.[36] This is in agreement with the evolution of magnetic transition fields under hydrostatic pressure that has been both theoretically analyzed and experimentally observed in related magnetic van der Waals materials.[23,37,38]

As for the Néel temperature shown in Figure 3c, mean field considerations predict that $T_N \propto H_F + H_E$ in the bulk limit.[39,40] Here, H_F is the intralayer ferromagnetic coupling, which would appear in a $-\frac{1}{2}H_F \sum_j M_j^2$ term in eq 1 and is assumed to be much stronger than the interlayer coupling ($H_F \gg H_E$). The contribution of anisotropy to T_N is negligible, in comparison. Therefore, the increase in H_E with pressure suggests an even greater decrease in H_F. Such an effect has been tied to the intralayer AFM interactions becoming stronger due to smaller Mn−Mn distances in the $a-b$ plane[33,36] and the changing Mn−Te−Mn bond angles, as it effectively decreases the FM coupling within the SL. The effect of disorder on the magnetic coupling strength is considered negligible compared to the influence of pressure-induced structural changes. This interpretation is consistent with our experimental observations. If we assume that the disorder density differs between the two devices, resulting in a small difference in the Néel temperature of about 2 K at ambient pressure, the changes observed under pressure are much larger, clearly indicating that the dominant contribution to the evolution of the magnetic coupling strength arises from the applied pressure rather than from disorder effects.

In light of the above, we can discuss the effect of pressure on the theoretically expected band gaps. The exchange energy of the top or bottom surface of the MBT crystal is $\sum_k M_k J_{s,k}$, where $J_{s,k}$ is the exchange coupling between the chosen surface and the kth layer.[11] Assuming only intralayer and nearest-neighbor interlayer exchange and using our previous notations, in the FM or AFM phase this sum is proportional to $H_F \pm H_E$. Neglecting tunneling between the surfaces or disorder, this predicts that the band gap in the FM phase is $\Delta_{CI} \propto H_F + H_E$. Its evolution with pressure based on Arrhenius analysis (Figure 5d at 0 and 1 GPa) qualitatively matches the trend of T_N in Figure 3c. As for the AFM gap, with the above assumptions, it is predicted to be $\Delta_A \propto H_F - H_E$ and indeed smaller than Δ_{CI}, although in the AFM phase disorder is expected to have a more important role, as discussed above, so the above assumption might be less valid. The difference between Δ_A and Δ_{CI} may be potentially even wider if the layer magnetizations are affected by field-polarizable defects. Therefore, an intermediate disorder potential may surpass Δ_A but not Δ_{CI}.

If the disorder is strong enough, then localization occurs in the device. In this respect, we expect that as the lattice constants decrease with pressure on the order of a few percent[33] and atomic wave functions overlap more and more, localization length ξ increases. Therefore, average activation energy Δ_0 of hopping transport will decrease.[41−43] According to Anderson localization, the conductivity increases with localization length: $\sigma_{xx} \propto \exp(-L_S/\xi)$, where L_S is the sample size. All of these are in good agreement with our experimental findings (Δ_0 in Figure 5d and $R_{xx} \propto \sigma_{xx}^{-1}$ in Figure 2), which suggests that pressure weakens the Anderson insulator state with an increase in localization length. At a sufficiently high pressure, the effect of disorder may become weak enough that it no longer overcomes AFM gap Δ_A. This would lead to the closure of Δ_0, the reopening of the nontrivial gap, and the recovery of the QAHE.[34] However, Δ_A also decreases with pressure due to both H_F and H_E, which may prevent the QAHE state.

While disorder appears to be the dominant limiting factor, subtle surface or interface asymmetry, particularly at the SiO_2/

https://doi.org/10.1021/acs.nanolett.5c05229
Nano Lett. 2026, 26, 1782−1788

MBT interface, may also play a small but non-negligible role in influencing the stability of the topological phase.

SUMMARY

Our study systematically explores the interplay among pressure, magnetism, and topology in a five-SL $MnBi_2Te_4$ film. At low fields in the AFM phase, the near-zero Hall resistance and high longitudinal and bulk resistance indicate a trivial insulator state likely due to disorder. When the FM phase is reached with an increase in the magnetic field, quantization is recovered. From the analysis of magnetic transition fields based on the magnetoresistance, we estimate that interlayer exchange coupling H_E is enhanced by hydrostatic pressure, while the decreasing Néel temperature suggests that intralayer coupling H_F is reduced. Although effective trivial band gap Δ_0 was also reduced, the quantum anomalous Hall effect was not recovered up to 2 GPa, indicating that this pressure is insufficient to fully overcome extrinsic effects such as disorder and interface imperfections.

These findings provide new insights into pressure-driven magnetic and topological transitions in $MnBi_2Te_4$, and they highlight that further advances in material quality and heterostructure design, including improved interface symmetry (e.g., through full hBN encapsulation), may be essential for realizing a robust QAHE in MBT-based systems.

ASSOCIATED CONTENT

Supporting Information

The Supporting Information is available free of charge at https://pubs.acs.org/doi/10.1021/acs.nanolett.5c05229.

Methods, additional experimental data, linear chain model, and transitions in the linear chain model (PDF)

AUTHOR INFORMATION

Corresponding Authors

Endre Tóvári − *Department of Physics, Budapest University of Technology and Economics, H-1111 Budapest, Hungary; MTA-BME Correlated van der Waals Structures Momentum Research Group, H-1111 Budapest, Hungary;* orcid.org/0000-0002-0000-3805; Email: tovari.endre@ttk.bme.hu

Péter Makk − *Department of Physics, Budapest University of Technology and Economics, H-1111 Budapest, Hungary; MTA-BME Correlated van der Waals Structures Momentum Research Group, H-1111 Budapest, Hungary;* orcid.org/0000-0001-7637-4672; Email: makk.peter@ttk.bme.hu

Authors

Albin Márffy − *Department of Physics, Budapest University of Technology and Economics, H-1111 Budapest, Hungary; MTA-BME Correlated van der Waals Structures Momentum Research Group, H-1111 Budapest, Hungary;* orcid.org/0000-0001-5343-453X

Yu-Fei Liu − *Department of Chemistry and Chemical Biology, Harvard University, Cambridge, Massachusetts 02138, United States; Department of Physics, Harvard University, Cambridge, Massachusetts 02138, United States*

Anyuan Gao − *Department of Chemistry and Chemical Biology, Harvard University, Cambridge, Massachusetts 02138, United States*

Tianye Huang − *Department of Chemistry and Chemical Biology, Harvard University, Cambridge, Massachusetts 02138, United States*

László Oroszlány − *Department of Physics of Complex Systems, ELTE Eötvös Loránd University, H-1117 Budapest, Hungary; Wigner Research Centre for Physics, H-1525 Budapest, Hungary*

Kenji Watanabe − *Research Center for Functional Materials, National Institute for Materials Science, Tsukuba 305-0044, Japan;* orcid.org/0000-0003-3701-8119

Takashi Taniguchi − *Research Center for Functional Materials, National Institute for Materials Science, Tsukuba 305-0044, Japan;* orcid.org/0000-0002-1467-3105

Su-Yang Xu − *Department of Chemistry and Chemical Biology, Harvard University, Cambridge, Massachusetts 02138, United States;* orcid.org/0009-0006-6819-3613

Szabolcs Csonka − *Department of Physics, Budapest University of Technology and Economics, H-1111 Budapest, Hungary; MTA-BME Superconducting Nanoelectronics Momentum Research Group, H-1111 Budapest, Hungary; HUN-REN Centre for Energy Research, H-1121 Budapest, Hungary*

Complete contact information is available at: https://pubs.acs.org/10.1021/acs.nanolett.5c05229

Notes

The authors declare no competing financial interest.

ACKNOWLEDGMENTS

This research was supported by the Ministry of Culture and Innovation and the National Research, Development and Innovation Office within the Quantum Information National Laboratory of Hungary (Grants 2022-2.1.1-NL-2022-00004 and UNKP-23-4-I-BME-36), by OTKA Grants K138433 and K134437, and by NKKP STARTING Grant 150232, EIC Pathfinder Challenge grant QuKiT. The authors acknowledge funding from the Multi-Spin and 2DSOTECH FlagERA networks, the 2DSPIN-TECH Flagship project, the Alexander von Humboldt Foundation, the European Research Council ERC project Twistrain, the TRILMAX Horizon Europe consortium (Grant 101159646), and COST Action CA 21144 superQUMAP. The work by the Xu group is supported by Air Force Office of Scientific Research (AFOSR) Grant FA9550- 626 23-1-0040. S.-Y.X. acknowledges the Sloan Foundation and Corning Fund for Faculty Development. K.W. and T.T. acknowledge support from the JSPS KAKENHI (Grants 20H00354 and 23H02052) and World Premier International Research Center Initiative (WPI), MEXT, Japan. Device fabrication was performed by Y.-F.L., A.G., and T.H. with the guidance of S.-Y.X. Measurements were performed by A.M. Experimental evaluation was done by A.M., and theoretical evaluation by E.T. and L.O. A.M. and E.T. wrote the paper and all authors discussed the results and worked on the manuscript. The project was guided by S.-Y.X., E.T., S.C., and P.M.

REFERENCES

(1) Yu, R.; Zhang, W.; Zhang, H. J.; Zhang, S. C.; Dai, X.; Fang, Z. Quantized anomalous hall effect in magnetic topological insulators. *Science* **2010**, *329*, 61−64.

(2) Chang, C.-Z.; Liu, C.-X.; MacDonald, A. H. Colloquium: Quantum anomalous Hall effect. *Rev. Mod. Phys.* **2023**, *95*, 11002.

(3) Ferreira, G. J.; Loss, D. Magnetically Defined Qubits on 3D Topological Insulators. *Phys. Rev. Lett.* **2013**, *111*, 106802.
(4) Zhang, D.; Shi, M.; Zhu, T.; Xing, D.; Zhang, H.; Wang, J. Topological Axion States in the Magnetic Insulator MnBi2Te4 with the Quantized Magnetoelectric Effect. *Phys. Rev. Lett.* **2019**, *122*, 206401.
(5) Otrokov, M. M.; et al. Prediction and observation of an antiferromagnetic topological insulator. *Nature* **2019**, *576*, 416−422.
(6) Otrokov, M. M.; Rusinov, I. P.; Blanco-Rey, M.; Hoffmann, M.; Vyazovskaya, A. Y.; Eremeev, S. V.; Ernst, A.; Echenique, P. M.; Arnau, A.; Chulkov, E. V. Unique Thickness-Dependent Properties of the van der Waals Interlayer Antiferromagnet MnBi2Te4 Films. *Phys. Rev. Lett.* **2019**, *122*, 107202.
(7) Ding, L.; Hu, C.; Ye, F.; Feng, E.; Ni, N.; Cao, H. Crystal and magnetic structures of magnetic topological insulators MnBi2Te4 and MnBi4Te7. *Phys. Rev. B* **2020**, *101*, 020412.
(8) Li, J.; Li, Y.; Du, S.; Wang, Z.; Gu, B.-L.; Zhang, S.-C.; He, K.; Duan, W.; Xu, Y. Intrinsic magnetic topological insulators in van der Waals layered MnBi2Te4-family materials. *Sci. Adv.* **2019**, *5*, eaaw5685.
(9) Liu, C.; Wang, Y.; Li, H.; Wu, Y.; Li, Y.; Li, J.; He, K.; Xu, Y.; Zhang, J.; Wang, Y. Robust axion insulator and Chern insulator phases in a two-dimensional antiferromagnetic topological insulator. *Nat. Mater.* **2020**, *19*, 522−527.
(10) He, K. MnBi2Te4-family intrinsic magnetic topological materials. *npj Quantum Mater.* **2020**, *5*, 90.
(11) Deng, Y.; Yu, Y.; Shi, M. Z.; Guo, Z.; Xu, Z.; Wang, J.; Chen, X. H.; Zhang, Y. Quantum anomalous Hall effect in intrinsic magnetic topological insulator MnBi2Te4. *Science* **2020**, *367*, 895−900.
(12) Chen, R.; Li, S.; Sun, H. P.; Liu, Q.; Zhao, Y.; Lu, H. Z.; Xie, X. C. Using nonlocal surface transport to identify the axion insulator. *Phys. Rev. B* **2021**, *103*, L241409.
(13) Wang, Y.; Fu, B.; Wang, Y.; Lian, Z.; Yang, S.; Li, Y.; Xu, L.; Gao, Z.; Jiang, W.; Zhang, J.; Wang, Y.; Liu, C. Towards the Quantized Anomalous Hall effect in AlO_x-capped $MnBi_2Te_4$. *Nat. Commun.* **2025**, *16*, 1727.
(14) Li, Y.; Liu, C.; Wang, Y.; Lian, Z.; Li, S.; Li, H.; Wu, Y.; Lu, H. Z.; Zhang, J.; Wang, Y. Giant nonlocal edge conduction in the axion insulator state of MnBi2Te4. *Science Bulletin* **2023**, *68*, 1252−1258.
(15) Ge, J.; Liu, Y.; Li, J.; Li, H.; Luo, T.; Wu, Y.; Xu, Y.; Wang, J. High-Chern-number and high-temperature quantum Hall effect without Landau levels. *National Science Review* **2020**, *7*, 1280−1287.
(16) Liu, C.; Wang, Y.; Yang, M.; Mao, J.; Li, H.; Li, Y.; Li, J.; Zhu, H.; Wang, J.; Li, L.; Wu, Y.; Xu, Y.; Zhang, J.; Wang, Y. Magnetic-field-induced robust zero Hall plateau state in MnBi2Te4 Chern insulator. *Nat. Commun.* **2021**, *12*, 4647.
(17) Ovchinnikov, D.; et al. Intertwined Topological and Magnetic Orders in Atomically Thin Chern Insulator MnBi2Te4. *Nano Lett.* **2021**, *21*, 2544−2550.
(18) Gao, A.; et al. Layer Hall effect in a 2D topological axion antiferromagnet. *Nature* **2021**, *595*, 521−525.
(19) Cai, J.; Ovchinnikov, D.; Fei, Z.; He, M.; Song, T.; Lin, Z.; Wang, C.; Cobden, D.; Chu, J. H.; Cui, Y. T.; Chang, C. Z.; Xiao, D.; Yan, J.; Xu, X. Electric control of a canted-antiferromagnetic Chern insulator. *Nat. Commun.* **2022**, *13*, 1668.
(20) Ying, Z.; Zhang, S.; Chen, B.; Jia, B.; Fei, F.; Zhang, M.; Zhang, H.; Wang, X.; Song, F. Experimental evidence for dissipationless transport of the chiral edge state of the high-field Chern insulator in MnBi2Te4 nanodevices. *Phys. Rev. B* **2022**, *105*, 085412.
(21) Li, Y. Reentrant quantum anomalous Hall effect in molecular beam epitaxy-grown MnBi2Te4 thin films. *arXiv* **2024**, DOI: 10.48550/arXiv.2401.11450.
(22) Zhang, S.; et al. Experimental Observation of the Gate-Controlled Reversal of the Anomalous Hall Effect in the Intrinsic Magnetic Topological Insulator MnBi2Te4 Device. *Nano Lett.* **2020**, *20*, 709−714.
(23) Chong, S. K.; Lei, C.; Li, J.; Cheng, Y.; Graf, D.; Lee, S. H.; Tanabe, M.; Yang, T.-H.; Mao, Z.; MacDonald, A. H.; Wang, K. L. Pressure tunable quantum anomalous Hall states in a topological antiferromagnet. *arXiv* **2023**, DOI: 10.48550/arXiv.2306.10325.
(24) Zhao, Y. F.; Zhou, L. J.; Wang, F.; Wang, G.; Song, T.; Ovchinnikov, D.; Yi, H.; Mei, R.; Wang, K.; Chan, M. H.; Liu, C. X.; Xu, X.; Chang, C. Z. Even-Odd Layer-Dependent Anomalous Hall Effect in Topological Magnet MnBi2Te4 Thin Films. *Nano Lett.* **2021**, *21*, 7691−7698.
(25) Garnica, M. Native point defects and their implications for the Dirac point gap at $MnBi_2Te_4(0001)$. *npj Quantum Mater.* **2022**, *7*, 7.
(26) Tan, H.; Yan, B. Distinct Magnetic Gaps between Antiferromagnetic and Ferromagnetic Orders Driven by Surface Defects in the Topological Magnet MnBi2Te4. *Phys. Rev. Lett.* **2023**, *130*, 126702.
(27) Li, Y.; et al. Fabrication-induced even-odd discrepancy of magnetotransport in few-layer MnBi2Te4. *Nat. Commun.* **2024**, *15*, 3399.
(28) Mei, R.; Zhao, Y. F.; Wang, C.; Ren, Y.; Xiao, D.; Chang, C. Z.; Liu, C. X. Electrically Controlled Anomalous Hall Effect and Orbital Magnetization in Topological Magnet MnBi2Te4. *Phys. Rev. Lett.* **2024**, *132*, 066604.
(29) Yang, S.; Xu, X.; Zhu, Y.; Niu, R.; Xu, C.; Peng, Y.; Cheng, X.; Jia, X.; Huang, Y.; Xu, X.; Lu, J.; Ye, Y. Odd-Even Layer-Number Effect and Layer-Dependent Magnetic Phase Diagrams in MnBi2Te4. *Physical Review X* **2021**, *11*, 011003.
(30) Chen, B.; Liu, X.; Li, Y.-H.; Tay, H.; Taniguchi, T.; Watanabe, K.; Chan, M. H. W.; Yan, J.; Song, F.; Cheng, R.; Chang, C.-Z. Even-Odd Layer-Dependent Exchange Bias Effect in MnBi2Te4 Chern Insulator Devices. *Nano Lett.* **2024**, *24*, 8320.
(31) Fülöp, B.; Márffy, A.; Tóvári, E.; Kedves, M.; Zihlmann, S.; Indolese, D.; Kovács-Krausz, Z.; Watanabe, K.; Taniguchi, T.; Schönenberger, C.; Kézsmárki, I.; Makk, P.; Csonka, S. New method of transport measurements on van der Waals heterostructures under pressure. *J. Appl. Phys.* **2021**, *130*, 064303.
(32) Bac, S. K.; et al. Topological response of the anomalous Hall effect in MnBi2Te4 due to magnetic canting. *npj Quantum Mater.* **2022**, *7*, 46.
(33) Chen, K. Y.; Wang, B. S.; Yan, J. Q.; Parker, D. S.; Zhou, J. S.; Uwatoko, Y.; Cheng, J. G. Suppression of the antiferromagnetic metallic state in the pressurized MnBi2Te4 single crystal. *Physical Review Materials* **2019**, *3*, 094201.
(34) Song, Z.-G.; Zhang, Y.-Y.; Song, J.-T.; Li, S.-S. Route towards Localization for Quantum Anomalous Hall Systems with Chern Number 2. *Sci. Rep.* **2016**, *6*, 19018.
(35) Zhang, J.; Chang, C.-Z.; Tang, P.; Zhang, Z.; Feng, X.; Li, K.; Wang, L.-l.; Chen, X.; Liu, C.; Duan, W.; He, K.; Xue, Q.-K.; Ma, X.; Wang, Y. Topology-Driven Magnetic Quantum Phase Transition in Topological Insulators. *Science* **2013**, *339*, 1582.
(36) Yan, J.-Q.; Okamoto, S.; McGuire, M. A.; May, A. F.; McQueeney, R. J.; Sales, B. C. Evolution of structural, magnetic, and transport properties in MnBi2-xSbxTe4. *Phys. Rev. B* **2019**, *100*, 104409.
(37) Pawbake, A.; et al. Magneto-Optical Sensing of the Pressure Driven Magnetic Ground States in Bulk CrSBr. *Nano Lett.* **2023**, *23*, 9587−9593.
(38) Song, T.; et al. Switching 2D magnetic states via pressure tuning of layer stacking. *Nat. Mater.* **2019**, *18*, 1298−1302.
(39) UryU, N. Phase transition in antiferromagnets with anisotropic exchange interactions and uniaxial anisotropy. *Phase Transitions* **1990**, *28*, 133−175.
(40) Johnston, D. C. Influence of uniaxial single-ion anisotropy on the magnetic and thermal properties of Heisenberg antiferromagnets within unified molecular field theory. *Phys. Rev. B* **2017**, *95*, 94421.
(41) Mott, N. F.; Davis, E. A. *Electronic Processes in Non-Crystalline Materials*, 2nd ed.; Oxford University Press: Oxford, U.K., 1979.
(42) Shklovskii, B. I.; Efros, A. L. *Electronic Properties of Doped Semiconductors*; Springer: Berlin, 1984.
(43) Pollak, M.; Shklovskii, B. I. *Hopping transport in solids*; Elsevier, 1991.

https://doi.org/10.1021/acs.nanolett.5c05229
Nano Lett. 2026, 26, 1782−1788